Supporting Information

Free Radical Generation from High Frequency Electromechanical Dissociation of Pure Water

Amgad R. Rezk,[†] Heba Ahmed,[†] Tarra L. Brain,[†] Jasmine O. Castro,[†] Ming K. Tan,[‡] Julien Langley,[¶] Nicholas Cox,[¶] Joydip Mondal,[§] Wu Li,[§] Muthupandian Ashokkumar,[§] and Leslie Y. Yeo[†]

[†]*Micro/Nanophysics Research Laboratory, School of Engineering, RMIT University, Melbourne, VIC 3000, Australia*
[‡]*School of Engineering, Monash University Malaysia, 47500 Bandar Sunway, Selangor, Malaysia*
[¶]*Research School of Chemistry, The Australian National University, Canberra, ACT 2601, Australia*
[§]*School of Chemistry, University of Melbourne, VIC 3010, Australia*

Email: leslie.yeo@rmit.edu.au

- Fabrication and characterisation of the surface acoustic wave (SAW) device
- Method for the sonoluminescence and sonochemiluminescence experiments
- Description of the numerical model used to simulate the SAW evanescent electric field
- Supplementary figures

Surface Acoustic Wave (SAW) Device Fabrication and Characterisation

The SAW device is schematically depicted in Fig. 1a in the main manuscript. Briefly, 45 finger pairs of 10 nm and 400 nm thick aluminium interdigital transducer (IDT) electrodes were patterned on a 0.5 mm thick single crystal piezoelectric lithium niobate ($LiNbO_3$; Roditi Ltd., London, UK) substrate using standard photolithography and wet etching. The finger width and gap d are set at 100 µm such that the wavelength of the SAW produced is $\lambda = 4d$ = 400 µm, corresponding to a SAW frequency of 10 MHz. The SAW is produced and propagates along the substrate when a sinusoidal electrical signal at this resonant frequency, generated using a RF signal generator (SML01; Rhode & Schwarz Pty. Ltd., North Ryde, NSW, Australia) and amplifier (ZHL-5W-1; Mini Circuits, Brooklyn, NY), is applied to the IDT. Voltage was monitored through an oscilloscope (Wavejet 332/334; LeCroy, Chestnut Ridge, NY). The resonance and impedance of the device was characterised using a network analyser (ZNB4; Rhode & Schwarz Pty. Ltd., North Ryde, NSW, Australia) whereas the SAW itself is visualised using a laser Doppler vibrometer (UHF-120; Polytec PI, Waldbronn, Germany).

The experiments were carried out in a 14 mm high enclosed microchamber, cut from a 3 mm internal diameter glass capillary, and glued onto the $LiNbO_3$ substrate 5 mm away from the IDT as illustrated in Fig. 1a. The top of the microchamber was sealed with paraffin film (Parafilm M, Sigma Aldrich Pty. Ltd., Castle Hill, NSW, Australia) to prevent gas dissolution into the sample from the ambient environment. The tips of the measurement probes were inserted into the sample by gently puncturing the film in order to maintain as best a seal around the probes as possible. All care was also taken to ensure the sample preparation, loading and subsequent withdrawal for analysis was conducted immediately and without exposure to air. A fresh sample was used for every experiment.

Preparation of Luminol Solution Under Various Gas Conditions

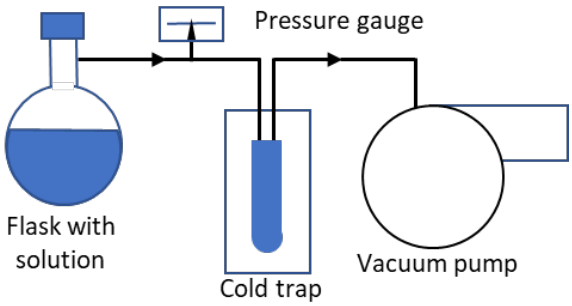

Figure S1. Schematic of the vacuum line for the degassing protocol.

The luminol solution was prepared based on the method described in [1]. Briefly, a 2 mM luminol solution (Sigma Aldrich Pty. Ltd., Castle Hill, NSW, Australia) was prepared in 0.1 M NaOH (Chem-Supply Pty. Ltd., Gillman, SA, Australia) solution in DI water (resistivity 18.2 MΩ.cm; Milli-Q, Merck Millipore, Bayswater, VIC, Australia). The solution was either placed as a sessile drop atop the $LiNbO_3$ substrate for immediate use (i.e., air-saturated condition), or subjected to further gas purging and degassing protocols. For the gas purging, 120 ml air-saturated 2 mM luminol solution was purged with nitrogen gas (>99.99% purity; BOC Gas, Preston, VIC, Australia) for 5 mins. The degassing process, on the other hand, was carried out with the vacuum setup shown in Fig. S1. The pressure was first reduced to 20 milliTorr using a vacuum pump (John Morris Scientific Pty. Ltd., Deepdene, VIC, Australia). The degassed solution was then transferred from the evacuated flask using a peristaltic pump (Longer Precision Pump Co. Ltd., Hebei, China) while minimising the introduction of air bubbles during the transfer. Two additional luminol samples under different gas conditions were prepared, namely, the air-depleted condition in which the sample was prepared with the degassing protocol, and the nitrogen-purged condition (i.e., with N_2 purging followed by degassing).

Sonoluminescence and Sonochemiluminescence Measurements

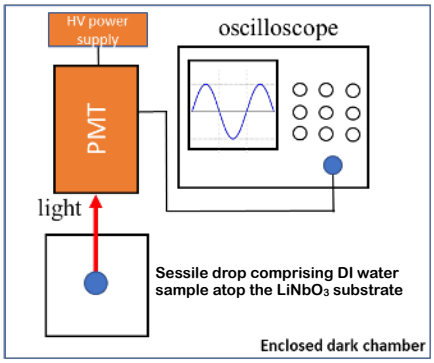

Figure S2. Schematic of the sonoluminescence and sonochemiluminescence measurement setup.

Both the sonoluminescence signal (if present) arising from any cavitation event generated by the acoustic forcing, as well as the sonochemiluminescence signal from the luminol reaction in the presence of any free radicals produced by the acoustic excitation, were detected using the setup shown in the Fig. S2 in which a photomultiplier tube ((PMT) Hamamatsu Photonics K.K., Hamamatsu City, Shizuoka Prefecture, Japan) connected to a high voltage (HV) photon amplifier (Hamamatsu) and oscilloscope (Wavejet 332/334; LeCroy, Chestnut Ridge, NY). If any photons were emitted from the sample and detected on the oscilloscope, a shift in the baseline signal was noted and recorded. This method was used for both sonoluminescence and sonochemiluminescence detection [1–3]. For standardisation, data requisition was conducted by averaging the signal over 32 sweeps. The baseline signal was recorded at the start of every set, after the sample was subjected to 10 s (unless otherwise stated) of acoustic excitation. By limiting the SAW irradiation within this duration, gas dissolution into the sample as well as temperature elevation effects on the chemiluminescence results was minimised. The experiments were repeated four times with a fresh sample to reach a consistent range for the result.

Numerical Simulations of the SAW and Associated Electric Potential and Field

In order to compute the evanescent electric field in the liquid droplet arising as a consequence of the SAW propagation in the piezoelectric substrate, we numerically solve in two-dimensional space (x_1, x_3) the equations of motion for the substrate vibration in coupling with the first order equation describing the propagation of the acoustic wave together with the conservation equation governing ion transport in the liquid; note that x_1 and x_3 correspond to the *x*- and *z*-axes, respectively, in the main text.

The time-domain constitutive equation governing the motion of a piezoelectric substrate to model the acoustic wave propagation in a solid are as follows:

$$\frac{\partial D_i}{\partial t} = e_{ijkl}\frac{\partial S_{kl}}{\partial t} + \varepsilon_{ik}^{\mathrm{S}}\frac{\partial E_k}{\partial t}, \tag{1}$$

$$\frac{\partial T_{ij}}{\partial t} = c_{ijkl}^{\mathrm{E}}\frac{\partial S_{kl}}{\partial t} - e_{kij}\frac{\partial E_k}{\partial t}, \tag{2}$$

wherein t denotes the time, e_{ijkl} are the piezoelectric stress coefficients, $\varepsilon_{ik}^{\mathrm{S}}$ the dielectric coefficients at constant strain $\mathbf{S}$, T_{ij} the stress components, c_{ijkl}^{E} the elastic stiffness coefficients at constant electric field E, and D_i the electric field displacement. In the quasistatic limit, the electromagnetic wave propagates much faster than the elastic wave and thus $\partial D_i/\partial t \approx 0$. Together with the infinitesimal strain-displacement relationship,

$$\frac{\partial S_{kl}}{\partial t} = \frac{1}{2}\left(\frac{\partial^2 \xi_k}{\partial x_l \partial t} + \frac{\partial^2 \xi_l}{\partial x_k \partial t}\right), \tag{3}$$

Eqs. (1) and (2) can be simplified such that

$$\frac{\partial E_k}{\partial t} = -\frac{e_{ijkl}}{\varepsilon_{ik}^{\mathrm{S}}}\left[\frac{1}{2}\left(\frac{\partial v_k}{\partial x_l} + \frac{\partial v_l}{\partial x_k}\right)\right], \tag{4}$$

$$\frac{\partial T_{ij}}{\partial t} = c_{ijkl}^{\mathrm{E}}\left[\frac{1}{2}\left(\frac{\partial v_k}{\partial x_l} + \frac{\partial v_l}{\partial x_k}\right)\right] - e_{kij}\frac{\partial E_k}{\partial t}, \tag{5}$$

where ξ and v are the displacement and velocity of the elements in the piezoelectric solid. Equations (4) and (5) can then be solved together with Newton's second law of motion,

$$\rho_{\mathrm{s}}\frac{\partial v_j}{\partial t} = \frac{\partial T_{ij}}{\partial t}, \tag{6}$$

to simulate the propagation of the acoustic wave in the solid.

To model the acoustic wave propagation in the liquid, we apply a regular perturbation expansion in the velocity $\mathbf{u}$, pressure p and density ρ fields in the asymptotically small limit $\epsilon \equiv U/c_0$, in which U represents the local characteristic velocity of the fluid elements and c_0 the speed of sound, to the equations governing the conservation of mass and momentum in the liquid, which, together with the equation of state, gives rise to the following first order approximation:

$$\frac{\partial \rho_1}{\partial t} + \rho_0(\boldsymbol{\nabla}\cdot\mathbf{u}_1) = 0, \tag{7}$$

$$\rho_0\frac{\partial \mathbf{u}_1}{\partial t} = -\boldsymbol{\nabla}p_1 + \mu\boldsymbol{\nabla}^2\mathbf{u}_1 + \left(\mu_{\mathrm{B}} + \frac{\mu}{3}\right)\boldsymbol{\nabla}\boldsymbol{\nabla}\cdot\mathbf{u}_1, \tag{8}$$

$$p_1 = c_0^2\rho_1, \tag{9}$$

in which μ and μ_{B} are the shear and bulk viscosities of the liquid, respectively. The zeroth term denoted by the subscript '0' refers to the unperturbed equilibrium state whereas first order approximations are denoted by the subscript '1', which represent the propagation of the sound wave in the fluid.

Finally, to model the transport of ions (in the absence of any chemical reactions) in the fluid medium, we solve the Nernst-Planck and Poisson equations:

$$\frac{\partial C_i}{\partial t} + \mathbf{u}_1 \cdot \boldsymbol{\nabla} C_i = \mathcal{D}_i \boldsymbol{\nabla}^2 C_i + \frac{z_i F D_i}{RT} \boldsymbol{\nabla} \cdot (C_i \boldsymbol{\nabla} \varphi), \tag{10}$$

$$\boldsymbol{\nabla}^2 \varphi = -\frac{\rho_\mathrm{e}}{\varepsilon_r \varepsilon_0}, \tag{11}$$

where C_i is the ionic concentration of species i, $\mathcal{D}_i$ the ion diffusivity, z_i the ion valency, T the temperature, φ the electric potential, ε_r the dielectric constant, ε_0 the permittivity of vacuum, $F = N_A e$ the Faraday constant and $\rho_\mathrm{e} = F \sum_i z_i C_i$ the charge density, in which N_A is Avogadro's constant and e the elementary charge. For deionised water at T = 293 K, $z_+ = z_- = 1$, $\mathcal{D}_1 = \mathcal{D}_2 = 1 \times 10^{-8}$ m^2/s, $\varepsilon_r \varepsilon_0 = 2.6 \times 10^{-10}$ C^2/J·m and the bulk ionic concentration $C_\infty = 10^{-7}$ M.

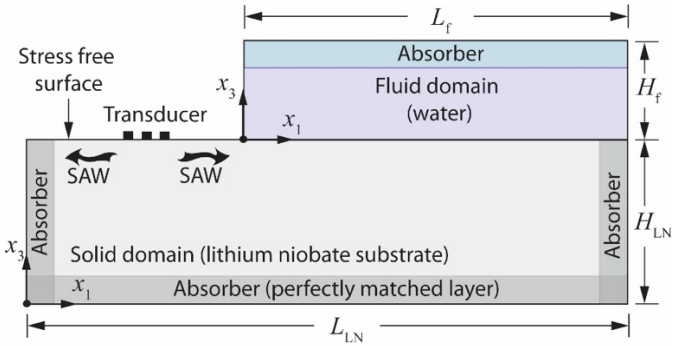

Figure S3. Schematic illustrating the computational domain employed in the numerical simulations, which comprise the piezoelectric solid (i.e., the lithium niobate substrate) on which the SAW propagates, and a fluid domain (i.e., deionised water) above it. The characteristic length and height scales of the solid and liquid domains are denoted by L_LN, H_LN, L_f and H_f, respectively.

The computational domain is shown in Fig. S3. Split-field perfectly matched layers (PMLs) are adopted in the solid and liquid domains to minimise wave reflection from the boundaries; the wave amplitude decays quadratically within the PMLs. To generate the SAW on the surface of the piezoelectric substrate, we impose a sinusoidal electric potential $\varphi = \varphi_{\mathrm{p-p}} \sin(2\pi x/\lambda_\mathrm{SAW}) \sin(\omega t)$, in which $\varphi_{\mathrm{p-p}}$ is the peak-to-peak voltage and $\omega = 2\pi f_\mathrm{SAW}$ the angular frequency. In the simulations, the SAW frequency f_SAW is set at 10 MHz and the peak-to-peak voltage is 10 V_{p-p}. At the solid–liquid interface, the domains are coupled through continuity in the velocities and stresses to allow full coupling of the mechanical motion between each domain. For the potential field in the fluid, we impose $\varphi_\mathrm{LN} = \varphi_\mathrm{f}$ and $\varepsilon_{33}\, \partial\varphi_\mathrm{LN}/\partial n = \varepsilon_\mathrm{f}\, \partial\varphi_\mathrm{f}/\partial n$, wherein φ_LN and φ_f are the potential in the piezoelectric substrate and the fluid, respectively. The far-field conditions, $\varphi_\mathrm{f} \to 0$ and $\partial\varphi_\mathrm{f}/\partial n \to 0$ also apply as $x_3 \to \infty$.

The size of the computational domain for the solid ($L_\mathrm{LN} \times H_\mathrm{LN}$) is approximately $6\lambda_\mathrm{SAW} \times 3\lambda_\mathrm{SAW}$, and the distance between the computational nodes is Δx_1 = Δx_3 = 4 μm. For the fluid domain, the computational domain ($L_\mathrm{f} \times H_\mathrm{f}$) is approximately $8\lambda_\mathrm{f} \times 3.5\delta_\mathrm{v}$, wherein λ_f is the sound wavelength in the liquid and $\delta_\mathrm{v} \equiv [2\mu/(\rho\omega_\mathrm{SAW})]^{1/2} \approx$ 170 nm the thickness of the viscous boundary layer; the distance between the computational nodes in the liquid domain is Δx_1 = 2 μm and Δx_3= 2 nm. To ensure numerical stability, the largest Courant number for the piezoelectric solid or liquid domains $C \equiv c\, \Delta t/\Delta x$ is selected to determine the maximum allowable time step Δt.

Equations (4)–(10) are solved simultaneously using a finite-difference time-domain method. At each time step Δt, the electric field is calculated through its decay away from the surface from the potential distribution in Eq. (11), which is solved using the Gauss-Seidel iterative procedure. Code validation of the SAW computations has been published in previous works [4–7].

Supplementary Figures

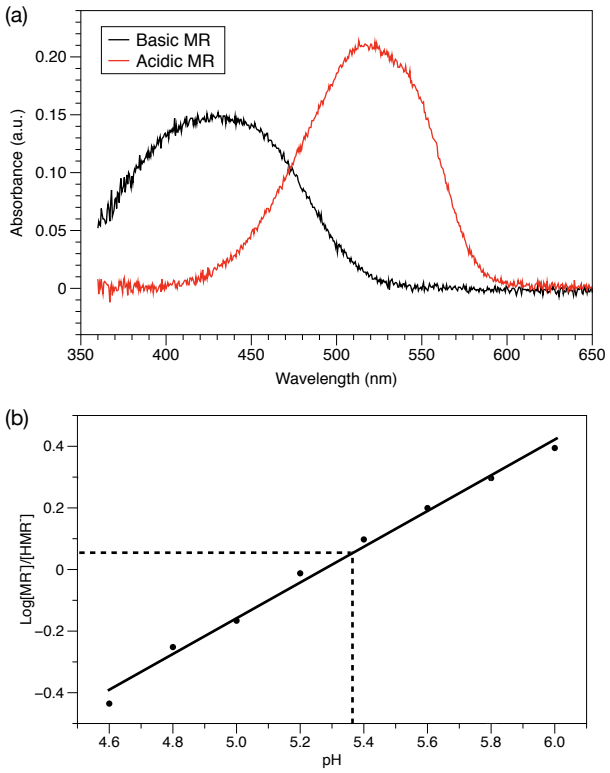

Figure S4. (a) Absorbance spectra of basic methyl red (MR^-) species obtained from 0.1 M sodium acetate solution at λ_{max} 435 nm, and that of acidic methyl red (HMR^-) obtained from 0.1 M acetic acid at λ_{max} 520 nm. (b) pH plot of 0.1 M acetate buffer standard solutions (pH 4.6 – 6) (solid line) and that for the deionised water sample following 10 s of SAW exposure (dotted line), obtained from the methyl red assay.

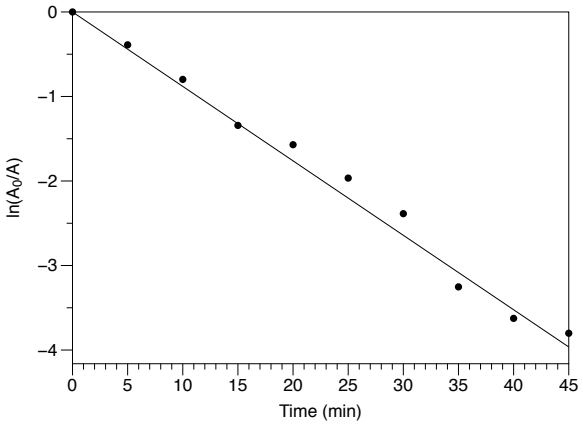

Figure S5. First order decomposition kinetics associated with the breakdown of the methylene blue dye upon its exposure to the SAW at an input voltage of 25 V_{rms}, as determined via absorbance measurements. A_o and A are the absorbance values for the untreated and treated samples, respectively.

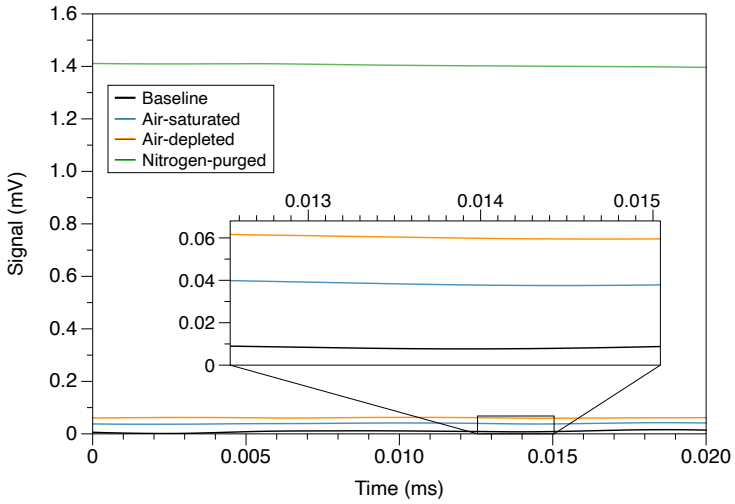

Figure S6. Luminol signal as a result of free radical generation in the sample, detected under a range of gas conditions. The air-saturated condition produced the weakest signal given the oxygen competition with the dye for the free radicals, while the nitrogen-purged sample (having the least amount of oxygen) produced the strongest signal. All results shown were for the signal emitted from the sample following 10 s of SAW exposure; for longer exposure times, the signals approached that of the air-saturated condition (not shown).

References

1. Ashokkumar, M.; Lee, J.; Iida, Y.; Yasui, K.; Kozuka, T.; Tuziuti, T.; Towata, A. Spatial Distribution of Acoustic Cavitation Bubbles at Different Ultrasound Frequencies. *ChemPhysChem* **2010**, *11*, 1680–1684.
2. Brotchie, A.; Grieser, F.; Ashokkumar, M. Effect of Power and Frequency on Bubble-Size Distributions in Acoustic Cavitation. *Phys. Rev. Lett.* **2009**, *102*, 084302.
3. Ashokkumar, M.; Guan, J.; Tronson, R.; Matula, T. J.; Nuske, J. W.; Grieser, F. Effect of Surfactants, Polymers, and Alcohol on Single Bubble Dynamics and Sonoluminescence. *Phys. Rev. E* **2002**, *65*, 046310.
4. Tan, M. K.; Yeo, L. Y.; Friend, J. R. Rapid Fluid Flow and Mixing Induced in Microchannels Using Surface Acoustic Waves. *EPL* **2009**, *87*, 47003.
5. Tan, M. K.; Friend, J. R.; Matar, O. K.; Yeo, L. Y. Capillary Wave Motion Excited by High Frequency Surface Acoustic Waves. *Phys. Fluids* **2010**, *22*, 112112.
6. Ang, K. M.; Yeo, L. Y.; Hung, Y. M.; Tan, M. K. Graphene-Mediated Microfluidic Transport and Nebulization via High Frequency Rayleigh Wave Substrate Excitation. *Lab Chip* **2016**, *16*, 3503–3514.
7. Ang, K. M.; Yeo, L. Y.; Hung, Y. M.; Tan, M. K. Acoustially-Mediated Microfluidic Nanofiltration Through Graphene Films. *Nanoscale* **2017**, *9*, 6497–6508.